CHAPTER 13

ANALYTICAL TECHNIQUES FOR STRUCTURAL CHARACTERIZATION OF BIOPOLYMER-BASED NANOCOMPOSITES

P. KUMAR, K. P. SANDEEP, S. ALAVI, and V. D. TRUONG

ABSTRACT

In recent years, biopolymer-based packaging materials have experienced a renewed industry and research focus. Such biopolymers include naturally occurring materials such as proteins, cellulose, and starches and synthetic materials such as polylactic acid that are manufactured from naturally derived monomers. Biopolymer-based packaging has the potential to replace plastics, as the latter are not only dependent on non-renewable resources such as petroleum for production but are also toxic to the environment. However, properties and performance of biopolymer-based packaging materials need much improvement. A new class of materials represented by biopolymer based nanocomposites or bio-nanocomposites have proven to be a promising option in this direction. Selection of proper techniques for characterization of these bio-nanocomposites is very critical in assessing their performance. This chapter reviews analytical techniques for the structural characterization of biopolymer-based nanocomposites, including X-ray diffraction, scanning electron micrsocopy, tunneling electron microscopy, atomic force microscopy, and spectroscopic techniques such as Fourier-transform infra-red and nuclear magnetic resonance. The relative strengths and drawback of these techniques are provided, and their application in understanding the interaction between nanoparticles and biopolymer matrix and synthesis of improved bio-nanocomposites is discussed.

13.1 INTRODUCTION

The non-biodegradable and non-renewable nature of plastic packaging has led to a renewed interest in packaging materials based on biopolymers derived from renewable sources. Such biopolymers include naturally occurring proteins, cellulose, starches, and other polysaccharides and those synthesized chemically from naturally derived monomers such as lactic acid. Commercialization of these bio-based polymers has already begun. Natureworks, LLC (Minnetonka, MN) manufactures polylactide from

corn sugar. The polymer can be hydrolyzed back to lactic acid. Wal-Mart stores Inc. is already using polylactide to package fresh-cut produce (Marsh and Bugusu, 2007). However, biopolymers cannot meet the requirements of a cost-effective film with mechanical and barrier properties matching those of plastics. Recently, a new class of materials represented by bio-nanocomposites has proven to be a promising option in improving the properties of these biopolymer-based packaging materials. Bio-nanocomposites consist of a biopolymer matrix reinforced with particles (nanoparticles) having at least one dimension in the nanometer range (1–100 nm). Bio-nanocomposites exhibit much improved properties as compared to biopolymers due to the high aspect ratio and high surface area of nanoparticles. Therefore, efforts have been geared towards developing bio-nanocomposites for food packaging films with improved mechanical, barrier, rheological, and thermal properties.

The most common class of materials used as nanoparticles are layered silicates such as clay minerals, graphite, and metal phosphates. Clay minerals such as montmorillonite (MMT), hectorite, sapnotite, and laponite have proven to be very effective due to their unique structure and properties. These clay minerals belong to the general family of 2:1 layered silicates indicating that they have 2 tetrahedral sheets sandwiching a central octahedral sheet (Zeng et.al., 2005). Paiva and et al. (2008) describe the properties, preparation, and applications of layered clays in detail. Biopolymers can be reinforced with these layered clays in order to enhance their properties while maintaining their biodegradability.

For preparation of a bio-nanocomposite, polymer chains must diffuse into the galleries between silicate layers to produce structures ranging from intercalated to exfoliated (Figure 1). There are four possible arrangements of layered clays dispersed in a polymer matrix – phase separated or immiscible (microcomposite), intercalated, exfoliated, and disordered intercalated (partially exfoliated). In an immiscible arrangement, platelets of layered clays exist as tactoids (stack of platelets separated by about 1 nm) and the polymer encapsulates these tactoids. Intercalation occurs when a monolayer of extended polymer chain penetrates into the galleries of the layered silicates. Intercalation results in finite expansion (2–3 nm) of the silicate layers. However, these silicate layers remain parallel to each other. Extensive penetration of polymer chains into the galleries of layered silicate leads to exfoliation or delamination of silicate layers. Clay platelets are separated by 10 nm or more during exfoliation. An exfoliated nanocomposite consists of nanoparticles distributed homogeneously throughout the polymer matrix (Dennis et.al., 2001; Zeng et al., 2005).

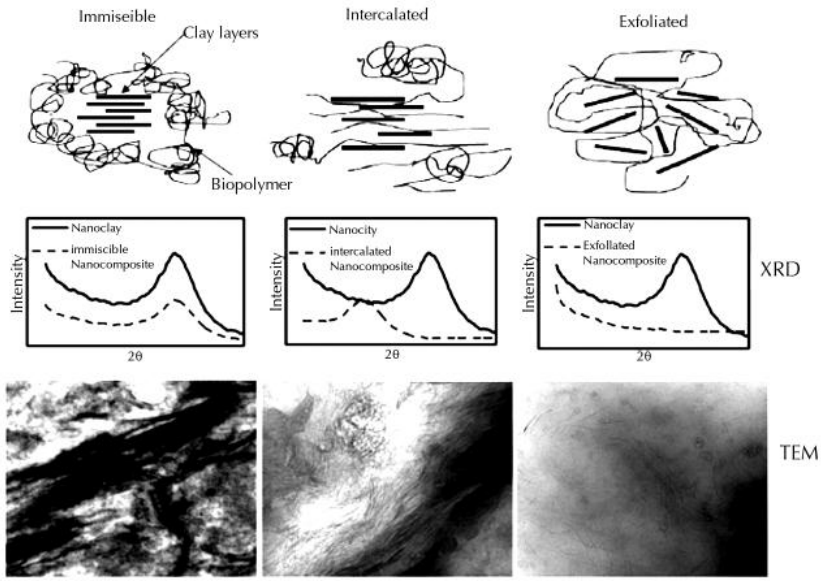

FIGURE 1 Possible arrangements of layered silicates in biopolymers with corresponding XRD and TEM results.

Bio-nanocomposites can be prepared by several methods which include *in situ* polymerization, solution exfoliation, and melt intercalation. In the *in situ* polymerization method, monomers are migrated into the galleries of layered silicates and subsequently polymerized via heat, radiation, or catalyst. In solution exfoliation, layered clays are exfoliated into single platelets. Exfoliation is achieved by dispersing the layered clays in a solvent. The polymer is adsorbed onto the platelets by mixing in the clay suspension. The solvent is removed either by evaporation or by precipitation. In melt intercalation, layered clays are mixed with the polymer matrix in molten state (Zeng et al., 2005).

Several review papers discuss the preparation, characterization, properties, and applications of bio-nanocomposites (Pandey et al., 2005; Ray and Bousmina, 2005; Yang et al, 2007; Rhim and Ng, 2007; Sorrentino et al., 2007; Zhao et al., 2008; Bordes et al., 2009). However, there is a lack of comprehensive review on various analytical techniques for the structural characterization of bio-nanocomposites. Selection of proper technique for characterization of these bio-nanocomposites is very critical in assessing their performance. A number of analytical techniques have been used to characterize the structure of bio-nanocomposites. These techniques include X-ray diffraction (XRD), microscopy transmission electron microscope (TEM), scanning electron microscope (SEM), scanning probe microscope (SPM), and confocal scanning laser microscope (CSLM), Fourier transform infra-red (FTIR) spectroscopy, and nuclear magnetic resonance (NMR). Each of the above mentioned techniques has its own benefits and limitations.

This chapter presents a review of analytical techniques for the structural characterization of bio-nanocomposites. A brief introduction of different techniques for the preparation of bio-nanocomposites is given. Analytical techniques for characterizing the structure of these bio-nanocomposites are discussed in terms of principle of operation, preparation of sample, interpretation of data, and limitations.

13.2 ANGLE X-RAY DIFFRACTION (WA-XRD)

X-rays were discovered in 1895 by W.C. Roentgen. When incident on a crystalline material, X-rays interfere with each other. This phenomenon is known as XRD. The WA-XRD is the most commonly used method to characterize the structure of bio-nanocomposites because of its ease of use and availability. The WA-XRD has been used to characterize dispersion of layered clays in nanocomposites based on protein (Chen and Zhang 2006; Shabeer et al., 2007; Yu et al., 2007) and starch (Dimonie et al., 2008; Tang et al., 2008).

PRINCIPLE OF OPERATION

X-rays are part of the electromagnetic spectrum with wavelength ranging from 0.01 to 10 nm. A schematic of an XRD instrument is shown in Figure 2. X-rays are generated by striking a pure anode of a metal (such as copper) with high-energy electrons in a sealed vacuum tube (X-ray tube). When a parallel and monochromatic X-ray beam with a wavelength of λ is incident on a sample (single crystal or powder ground to size less than 50 μm), the beam is transmitted, absorbed, refracted, scattered, and diffracted. A detector is used to measures the intensity of the diffracted X-rays in counts per second (cps). The sample may be set at any desired angle (θ) to the incident beam. For WA-XRD, the value of 2θ is greater than 1°. A diffraction plot detects the intensity of diffracted X-rays as a function of 2θ. Sharp peaks, corresponding to the interlayer spacing, are seen on the diffraction data. These peaks are characteristic to the material and the structure of the crystal. From the diffraction data, interlayer spacing (d-spacing or d) between clay layers is estimated from Bragg's equation (Kasai and Kakudo, 2005):

$$d = \frac{\lambda}{2\sin\theta} \text{ * MERGEFORMAT} \quad (1)$$

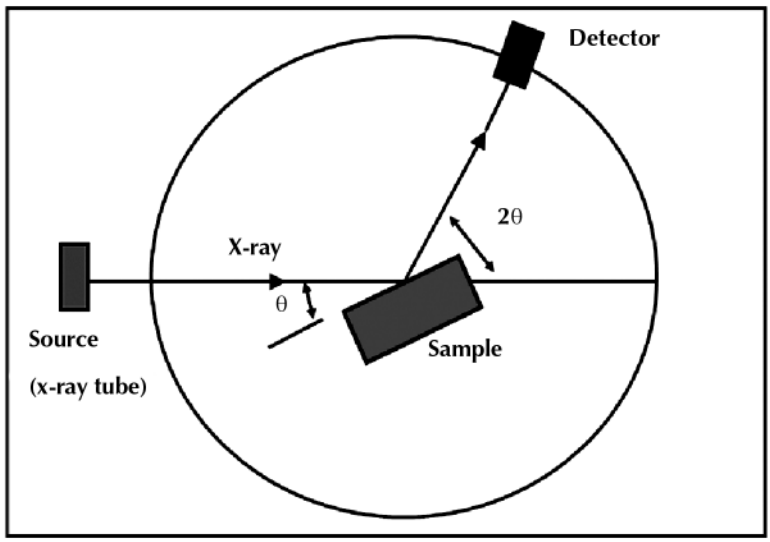

FIGURE 2 A schematic of an XRD instrument.

PREPARATION OF SAMPLES

Bio-nanocomposite samples for XRD analysis should be well ground to a particle size of less than 50 μm. Uniform particle size and random orientation of crystals are very critical for accurate XRD analysis. A sample with well-defined orientation of crystals (preferred orientation) can give a different diffraction pattern than that of a sample with randomly oriented crystals. Preferred orientation is particularly a problem with plate like crystals because they tend to lie horizontal, rather than perpendicular, on the sample holder. For a film sample, the thickness of the film should be at least 0.5 mm in order to detect the intensity of diffracted X-rays. The XRD analysis should be sensitive enough to detect the crystalline structure of layered silicates present in small amounts in bio-nanocomposites (Kasai and Kakudo, 2005).

COLLECTION AND INTERPRETATION OF DATA

Diffraction pattern for a particular sample is obtained by plotting the intensity of diffracted X-rays as a function of 2θ. Bio-nanocomposites are characterized by monitoring the intensity, width, and position of the peak in the diffraction pattern. Intensity of the peak provides information about the location of atoms in the unit cell. Higher intensity corresponds to higher electron density around the atom. Peak width provides information on the size of crystal and imperfections in the crystal. Peak width increases as the size of the crystal decreases. Position of the peak is used to estimate interlayer spacing by using the Bragg's equation as mentioned above.

The XRD patterns for various possible arrangements of layered silicates in biopolymers are shown in Figure 1. For an immiscible arrangement (microcomposite) of layered clays in a biopolymer matrix, the structure of the layered silicate in the composite is not affected. Thus, XRD pattern for the microcomposite should remain same as that obtained for the pure layered silicate. Intercalation of the polymer

chains increases the interlayer spacing and according to Bragg's law, it causes a shift of the diffraction peak towards lower 2θ angle. As more polymers enter the interlayer spacing, the clay platelets become disordered, thus causing broader peaks and a wider distribution of such peaks. For exfoliated nanocomposites, there is no peak in the diffraction pattern because of the much larger interlayer spacing (>8–10 nm) between the silicate layers (McGlashan and Halley, 2003; Pavlidou and Papaspyrides, 2008; Paul and Robeson, 2008).

LIMITATIONS

The XRD is a simple and convenient method to determine d-spacing for immiscible or intercalated arrangements of layered silicates in bio-nanocomposites. However, it may be insufficient to characterize exfoliated nanostructures. Absence of peak in diffraction pattern is often misinterpreted as an indication of exfoliation. Other than exfoliation, dilution, and preferred orientation of clay in nanocomposites might result in a diffraction pattern with no peak. The XRD cannot be used to determine the spatial distribution and dispersion of layered silicates in bio-nanocomposites (Morgan and Gilman 2003). Therefore, XRD should always be used in conjunction with some other techniques such as TEM, SEM, or AFM.

Wide-angle XRD is not useful to study intercalation once the d-spacing exceeds 6–7 nm. However, small-angle (2θ< 1°) X-ray diffraction (SA-XRD) analysis in combination with WA-XRD can be useful for characterization of such intercalated nanocomposites (Ray and Bousmina, 2005).

13.3 MICROSCOPY

Microscopy is the study of objects that are smaller than the spatial resolution (~75 μm) of human eye. Spatial resolution is the minimum possible length of an object which could be seen and separately identified from an adjacent and similar object. Light microscopes were developed in the early 17th Century. The spatial resolution (δ) of a light microscope can be approximated by the classical Rayleigh criterion as (Williams and Carter, 1996):

$$\delta = \frac{0.61\lambda}{\mu \sin\beta} \quad \backslash^* \text{ MERGEFORMAT (2)}$$

where λ is the wavelength of the radiation, μ is the refractive index of the viewing medium, and β is the semi-angle of collection of the magnifying lens. Wavelength for the light in the middle of the visible spectrum is ~ 550 nm. This gives light microscopes a resolution of approximately 300 nm. Early in the 20th Century, the wavelike nature of electrons was discovered. The electrons have a much lower wavelength as compared to that of light. Therefore, it is possible to achieve a resolution of as low as 0.2 nm by using electrons as a radiation source.

13.3.1 TRANSMISSION ELECTRON MICROSCOPE (TEM)

Transmission electron microscope was developed by Max Knoll and Ernst Ruska in 1931. In addition to XRD, TEM images provide further evidence for the occur-

rence of intercalation or exfoliation in nanocomposites. The TEM allows a qualitative understanding of the internal structure, spatial distribution, and dispersion of the nanoparticles within polymer matrices that are thin (< 100 nm) enough to transmit electrons.

PRINCIPLE OF OPERATION

Transmission electron microscope operates on the same basic principles as the light microscope but uses electrons instead of light. The TEM uses electrons as the radiation source and their much lower wavelength (in the order of one-tenths of a nanometer) makes it possible to achieve a resolution (0.2 nm) which is thousand times better than that of a light microscope. A schematic representation of a transmission electron microscope is shown in Figure 3. A TEM instrument can be divided into three sections: illumination system, specimen stage, and imaging system. The illumination system comprises of an electron gun, two or more condenser lens, and a condenser aperture. The specimen stage allows samples to be held for the analysis. The imaging system consists of an objective lens, an objective aperture, one or more intermediate lens, a projector lens, and a screen (Egerton, 2005).

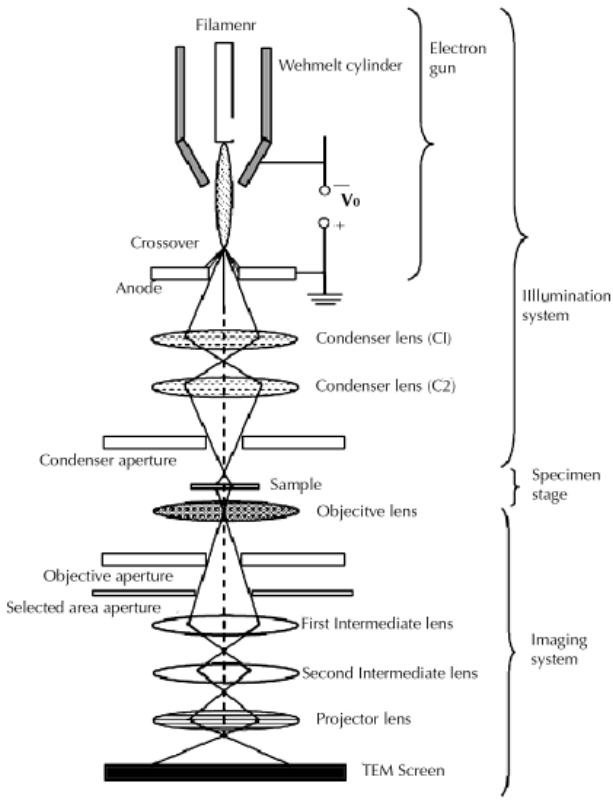

FIGURE 3 A schematic representation of a transmission electron microscope (adapted from Egerton 2005).

A fine beam of electrons with precisely controlled energy is produced in the electron gun. The gun consists of an electron source (filament for thermionic emission) and an accelerating chamber. The filament is made from a high melting point material such as tungsten. Once heated to a temperature above 2700K, the tungsten filament emits electrons into the surrounding vacuum. Wehnelt cylinder is a metal electrode which surrounds the filament except for a small opening through which the electron beam emerges. Wehnelt cylinder controls the emission current of the electron gun. After emission, electrons are accelerated by applying a potential difference (accelerating voltage), V_0 (100–500 kV) between the cathode and anode. Accelerating voltage determines the velocity and wavelength of the electron beam. Only 1% of the accelerated electrons are able to pass through the anode plate. Crossover is the effective source of illumination for the TEM. The first condenser lens (C1), which is a strong magnetic lens, creates a demagnified image of the electron beam. It also controls the minimum spot size available in the rest of the condenser system. The second condenser lens (C2), which is a weak magnetic lens, is used to vary the diameter of illuminated area of the sample. Condenser aperture controls the fraction of electron beam which illuminates the sample. Once the electron passes through the sample, the objective lens forms an inverted image. Objective aperture improves the contrast of the final image by passing only those electrons which will contribute to the final image. It also limits the blurring of image that arises from spherical and chromatic aberration. The purpose of the intermediate lens is to magnify the initial image formed by the objective lens. The intermediate lens can also be used to produce an electron diffraction pattern on the TEM screen. Projector lens produces an image or a diffraction pattern on the TEM screen. The TEM screen is used to convert the electron image to a visible form. It consists of a metal plate with a coating of $ZnSO_{4,}$ which emits visible light under electron bombardment (Egerton, 2005).

The combination of TEM with other analytical techniques such as energy dispersive X-ray spectroscopy (EDS) and electron energy loss spectroscopy (EELS) can generate information for image analysis and chemical composition of the sample. The EELS can also provide information on the electronic structure of the sample (Koo, 2006). Some new developments in TEM for nanotechnology have been reviewed by Wang (2003). Transmission electron microtomography (TEMT) is an emerging three-dimensional imaging technique with a sub-nanometer resolution (~0.5 nm). Three-dimensional image obtained from TEMT can help in understanding the relationship between the structure and property of bio-nanocomposites (Jinnai and Spontak, 2009).

PREPARATION OF SAMPLES

Samples should be thin (< 100 nm) enough to transmit electrons and stable to electron bombardment under high vacuum. Typically, samples are made circular with a diameter of 3 mm. The sample must be inserted into the vacuum of the TEM column without introducing air. Samples are most commonly prepared by either ultramicrotomy or focused ion beam (FIB).

The TEM samples are prepared by cutting ultra thin (< 100 nm) sections from a small block of embedded material using ultramicrotomy. Ultramicrotomy is high precision cutting method using glass or diamond knife. The cut sections are floated onto a water surface. A fine-mesh copper grid (diameter of 3 mm) is then introduced below

the surface of water. The grid is slowly raised and the cut section is supported by the grid. After drying in air, the ultra thin section remains attached to the grid. To produce scattering contrast, the cut section is stained by immersing in a solution of heavy metal (Egerton, 2005).

Focused ion beam (FIB) milling is a technique that uses a beam of accelerated ions to modify materials with nanometer precision. A schematic representation of a focused ion beam instrument is shown in Figure 4. A FIB instrument operates similar to an SEM. The FIB utilizes a liquid metal ion source (LMIS) at the top of its column to produce ions (usually Ga^+). The ions are focused into a beam by an electrostatic lens. After passing through the aperture and objective lens, the ion beam scans the surface of the sample. A beam diameter of 5–0.5 μm can be achieved in a FIB. The collision of ions with the atoms of the sample can be either elastic or inelastic in nature. An elastic collision results in removal of surface atoms. Removal of atoms, which is known as sputtering, modifies the surface of the sample. During inelastic collision, ions transfer a part of their energy to either surface atoms or electrons. Inelastic collision produces secondary electrons along with X-rays. The intensity of secondary electrons at each scan position can be used to create an image of the sample. Over an extended period of time, the sputtering process leads to noticeable removal of material. This is used for milling and probing applications. The small beam size in FIB makes it ideal for preparation of samples for TEM and SEM (Giannuzzi and Stevie, 1999; Yao, 2005).

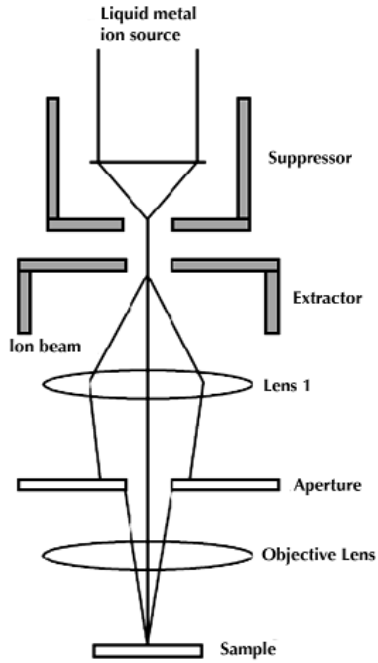

FIGURE 4 A schematic representation of a focused ion beam instrument (adapted from Guiannuzzi and Stevie 1999).

Samples of nanocomposite powders can be prepared by suspending the powder in a volatile solvent such as acetone. A drop of the suspension is then put on a fine-mesh copper grid. After drying in air, the nanocomposite powder remains attached to the grid and can be viewed under the TEM.

COLLECTION AND INTERPRETATION OF DATA

An ideal TEM image should have a good resolution and contrast. For bio-nanocomposites, contrast arises from differences in the atomic number of the layered silicates and the biopolymer matrix. Layered silicates with high atomic number appear dark in TEM image. The TEM results are quantified by the TEM particle density (number of platelets per unit area). The extent of exfoliation is better for samples with higher TEM particle density. Particle density per unit nanoparticles concentration is known as the specific particle density (Chavaria el al., 2004). However, it is difficult to calculate the TEM particle density for intercalated and partially exfoliated nanocomposites. Nam et al., (2001) calculated the length, thickness, and correlation length of the dispersed clay particles from TEM images. Correlation length was defined as the inter-particle distance in the direction perpendicular to that of the length of clay layers. Vermogen et al., (2005) proposed a method for quantifying TEM micrographs by measuring the length (L), thickness (t), and aspect ratio of clay layers. Inter-particle distance ($\varepsilon_{\parallel}$) in the direction parallel to that of the length of clay layers and inter-particle distance ($\varepsilon_{\perp}$) in the direction perpendicular to that of the length of clay layers were also measured.

The number (N) of platelets in an intercalated layered silicate was calculated as:

$$N = \frac{t_p + d - t_{platelet}}{d} \quad \backslash* \text{ MERGEFORMAT} \tag{3}$$

where t_p is the thickness of the particle, d is the interlayer spacing, and $t_{platelet}$ is the thickness of a single platelet. Six classes of tactoids based on thickness were defined. These tactoids ranged from individual exfoliated sheet to micron size aggregate. The TEM has been used to characterize dispersion of layered clays in nanocomposites based on protein (Chen and Zhang 2006; Yu et al., 2007) and starch (Tang et al., 2008).

LIMITATIONS

A TEM instrument is more expensive than an XRD instrument. Methods for sample preparation are tedious. Only a small portion of the sample can be viewed. Samples containing water cannot be viewed under TEM because of the high vacuum in the sample chamber. The TEM results are difficult to quantify because TEM provides two-dimensional images of a three-dimensional sample. If the sample is not made very thin, electrons can be scattered or absorbed, rather than transmitted (Williams and Carter, 1996). Proper experimental conditions such as low exposure times and high accelerating voltage are necessary to prevent decomposition of the clay structure in the nanocomposites (Monticelli et al., 2007).

13.3.2 SCANNING ELECTRON MICROSCOPE (SEM)

The SEM is a type of microscope that uses high energy beam of electrons instead of light to scan surface of a relatively thick sample. SEM has a resolution of 1–10 nm.

PRINCIPLE OF OPERATION

A schematic representation of a scanning electron microscope is shown in Figure 5. Similar to TEM, an SEM incorporates an electron gun to generate a beam of electrons. The maximum accelerating voltage in SEM is typically 30 kV, which is lower than that in TEM (100–500 kV). The electron beam is demagnified by the first condenser lens (C1). The condenser aperture eliminates high-angle electrons by constricting the beam. The second condenser lens forms a thin and coherent beam. An objective aperture further eliminates high-angle electrons from the beam. The objective lens focuses the electron beam into a small-diameter (1–10 nm) electron probe. Electrons (primary) incident on a sample supply enough energy to the atomic electrons (secondary) present on the surface of the sample so that they can be released. A small fraction of primary electrons are elastically back-scattered (angle of deflection >90°) with only a small loss in energy. Due to their high energy, these back-scattered electrons (BSEs) can re-enter the surrounding vacuum. However, the secondary electrons can be distinguished from the backscattered electrons because of their much lower energy. A set of coils scans the electron beam over the sample in two perpendicular directions and covers a square or rectangular area of the sample. This procedure is known as raster scanning. An image of the raster is formed by sequential collection of secondary electrons from each scanned point. Thus, the image in SEM is generated sequentially rather than simultaneously as in TEM (Egerton, 2005).

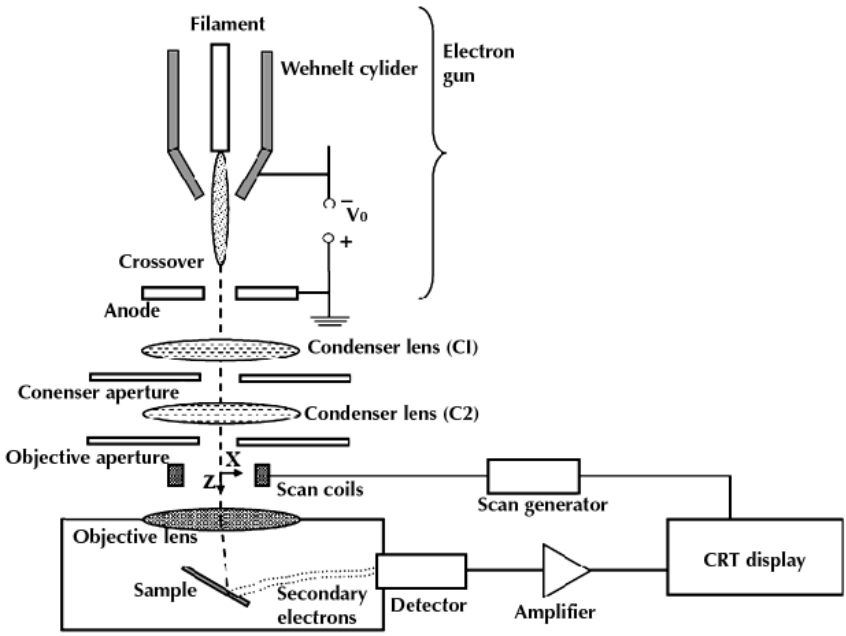

FIGURE 5 A schematic representation of a SEM (adapted from Egerton 2005).

PREPARATION OF SAMPLES

One major advantage of SEM over TEM is the ease of sample preparation. A sample does not need to be made thin. Conducting materials require no special sample preparation for SEM. Samples of insulating materials become charged when exposed to the electron probe. Negatively charged samples repel incident electrons, resulting in image distortion. Therefore, insulating materials are coated with a thin (15–40 nm) layer of metal (gold, chromium, and palladium) or conducting carbon. This process of coating is known as sputter coating. In sputter coating, the specimen chamber is exposed to very low vacuum (~0.1 Pa). An inert gas such as Argon (Ar) is introduced in the chamber. Gas molecules are ionized into ions and electrons because of the high voltage applied to the chamber. When struck with ions, the target metal ejects atoms. Atoms collide with residual gas molecules and deposit on the sample. Some of the limitations of the sputter coating process are thermal damage and surface contamination of the specimen. Sputter coating also reduces the penetration depth of SEM because of the thickness of the coating (Bozzola and Russell, 1999).

When coating is undesirable or difficult, low voltage should be used to avoid charging of the sample. An alternative to overcome charging of the samples is to surround the sample with a gaseous environment (low vacuum of up to 4000 Pa) rather than high vacuum (~10^{-4} Pa). This type of SEM is known as low-vacuum SEM or environmental SEM (ESEM). However, vacuum must be maintained in environmental SEM column for the operation of electron gun, acceleration of electrons, and focusing of electrons. After being focused by the objective lens, primary electrons ionize gas molecules (usually water vapor) before reaching the sample. Ionized gas molecules neutralize the surface charge of the sample. The pressure in the sample chamber can be as high as 5000 Pa (Egerton, 2005).

The SEM has also been used to study the fractured surface (cross-section) of bionanocomposite films (Vaz et al., 2002; Yu et al., 2007). Sample of fractured surface is prepared by freezing the film in liquid nitrogen, followed by breaking the film to expose the fracture surface, and sputter coating the fractured surface with a conducting coating (Yu et al., 2007).

COLLECTION AND INTERPRETATION OF DATA

The SEM images can be used to study the surface morphology of a material. A smooth surface can be distinguished from a rough surface by visual inspection. Comparatively larger (~1 μm) aggregates of nanoparticles at the surface can be observed in the SEM image. The SEM images can be used as a quick method to study the formation of nanocomposite structure.

LIMITATIONS

An image from SEM represents only the property of a surface and not the internal structure that is visible with a TEM image. The process of generating an image in SEM is slower than that in TEM. The SEM cannot be used to study detailed structure of nanocomposites because it has a poorer resolution as compared to TEM. Therefore, SEM analysis should always be used in combination with other microscopic techniques such as TEM or AFM.

SCANNING PROBE MICROSCOPE (SPM)

The use of a probe can resolve atoms as the resolution is no longer restrained by the wavelength of light or electrons. A probe can also be used to manipulate the structures along with scanning them. Some examples of SPM are scanning tunneling microscope (STM) and atomic force microscope (AFM).

13.3.3 SCANNING TUNNELING MICROSCOPE (STM)

Gerd Binnig and Heinrich Rohrer invented the scanning tunneling microscope in 1982, which gives three-dimensional images of conducting objects down to the atomic level. A spatial resolution of 0.01 nm can be achieved with a STM.

PRINCIPLE OF OPERATION

A schematic representation of a scanning tunneling microscope is shown in Figure 6. A very sharp metallic tip (M) is fixed on top of a piezodrive (P_z) to control the height (s) of the tip above the surface of a sample. The tip is brought within about 0.3–1 nm of the sample and a small potential difference ($V_t \sim 0.01–1$ V) is applied. Electrons move between the tip and the conducting sample by the process of quantum-mechanical tunneling. Quantum- mechanical tunneling is an effect of the wavelike nature of electrons which allows them to pass through small barriers such as the vacuum barrier between the tip and the sample. The amount of electrical current (tunneling current, J_t) flowing between the tip and the sample is measured. The tunneling current is very sensitive to the distance between the tip and the surface. A feedback control unit (CU) is used to adjust the height of the tip so that the tunneling current (J_t) remains constant. Two other piezodrives (P_x and P_y) are used to scan the tip in the lateral dimensions. During scanning of the surface, voltage (V_p) supplied to P_z is recorded as an image. This mode of operation is known as constant current mode and is mostly used to scan rough surfaces. In the constant height mode, the tip height (s) above the surface is kept constant and the variation of tunneling current reflects the corrugation of the surface (Bhushan 2004; Jia et al., 2005; Egerton 2005).

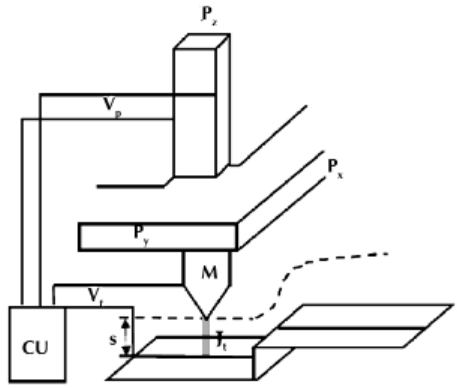

FIGURE 6 A schematic representation of a scanning tunneling microscope (adapted from Jia et al., 2005).

PREPARATION OF SAMPLES

Samples must be conductive enough to allow sufficient tunneling current (0.2–10 nA), which can be measured. Insulating samples can be coated with a thin layer of a conducting material and visualized with an STM (Bhushan, 2004).

COLLECTION AND INTERPRETATION OF DATA

The STM images can be interpreted in a manner similar to that for AFM, as discussed in the section under atomic force microscope.

LIMITATIONS

The main limitation of STM is that it can only take images of conducting or semiconducting surfaces under ultra high vacuum. It requires great mechanical precision to maintain a tip within 1 nm of a surface. An STM can provide structural information of only the surface of a sample. Therefore, it should be combined with some other technique such as TEM.

13.3.4 ATOMIC FORCE MICROSCOPE (AFM)

Gerd Binnig, Calvin Quate, and Christoph Gerber invented the atomic force microscope in 1985. Similar to an SEM, AFM can produce very high resolution three-dimensional images of the surface of a sample. The advantages of AFM include low cost, ease of use, and ease of sample preparation. The AFM does not require the sample to be conducting. Therefore, AFM can be used to take images of any type of surfaces including polymers, ceramics, composites, glass, and biological samples.

PRINCIPLE OF OPERATION

A schematic representative of an atomic force microscope is shown in Figure 7. A probe (cantilever with a sharp tip) is brought very close to the surface of a sample and the interatomic force between the probe tip and the sample is monitored. The interatomic force is repulsive if the tip is in direct contact with the sample. At a small distance above the sample, the tip senses an attractive van der Waals force. The interatomic force is determined by precisely measuring the displacement of the cantilever. A laser beam, which is deflected from the back of the cantilever, is directed to a photodetector. The photodetector measures the normal and lateral deflections of the cantilever. The deflections of the cantilever are converted into an image. A feedback control unit (CU) is used to adjust the height of the tip so that the interatomic force remains constant. A scanner is used for three-dimensional movement of the probe or sample in AFM. The scanners are made of piezoelectric materials to provide precise positioning in the nanometer range. There are two main modes of operation in AFM: contact mode and tapping or intermittent contact mode. The tip remains in permanent contact with the sample in contact mode. The force between the tip of the cantilever and the sample is measured at each point on the surface. A feedback loop keeps the force at a constant value by adjusting the height of the surface relative to the cantilever. The change in height is used to determine the topography of the surface. In tapping mode, the cantilever tip is oscillated above the surface of the sample at its resonant frequency. Oscillation of the cantilever is reduced because contact between tip and the surface results in loss of energy. The reduction in amplitude of oscillation is used to determine

the topography of the surface. The tapping mode works well with soft materials that might be damaged in contact mode (Bhushan 2004; Magonov and Yerina, 2005).

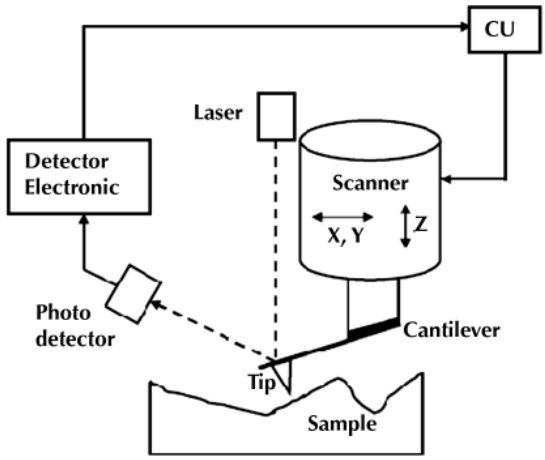

FIGURE 7 A schematic representation of an atomic force microscope (adapted from Magonov and Yerina 2005).

PREPARATION OF SAMPLES

Unlike other microscopy techniques, preparation of sample is quite simple in AFM. Samples do not require staining as in TEM or conductive coating as in SEM. Surface of the sample should be free of any scratches and foreign particles. Flat surfaces of samples can be prepared by ultramicrotoming (Yalcin and Cakman, 2004).

The AFM is typically conducted at ambient conditions. However, AFM can also operate with its tip and sample immersed in a liquid such as water. This makes AFM very useful in taking images of biological samples (Egerton, 2005). The AFM measurements at elevated temperatures of 150–300°C are now possible and AFM analysis can also be performed below 0 °C. The AFM imaging at elevated temperatures can be used to study structural changes in materials related to different thermal transitioning such as melting, crystallization, recrystallization, and glass transition (Ivanov et al., 2001; Magonov and Yerina, 2005).

COLLECTION AND INTERPRETATION OF DATA

The AFM images can be used to study detailed structure of the surface of a sample. The basic measurement in AFM is deflection of the cantilever over each x and y coordinates of the surface. This data can be used to define an average roughness (R_a) of the surface as (Ghanbarzadeha and Oromiehib 2008):

$$R_a = \frac{\sum_{i=1}^{N}\left(Z_i - \overline{Z}\right)}{N} \quad \backslash^* \text{ MERGEFORMAT} \tag{4}$$

where Z_i is the deflection value, $\overline{ZZ}$ is the arithmetic mean of deflection values, and N is the number of x and y coordinates of the surface.

The AFM can also be used to determine adhesive and mechanical properties of a surface on nano-scale. The force required to pull the tip from the surface can be used as a quantitative measure of the adhesion between tip and surface. The mechanical response of the surface can be determined by using AFM in the contact mode at different force levels (Magonov and Renekar, 1997).

LIMITATIONS

The AFM can be used to study only the surface of a sample. Mechanical scanning of a large area of a sample in AFM is very time consuming. The probing of materials with AFM is based on mechanical interactions. This prevents AFM from being used for studying the chemical nature of materials. Another limitation of AFM is due to the finite size and shape of the probe. The AFM cannot be used to analyze a surface which has nanoparticles with dimensions smaller than the probe itself.

13.3.5 CONFOCAL SCANNING LASER MICROSCOPE (CSLM)

The CSLM is a non-destructive optical microscopic technique for the study of a material surface or internal structure of semi-transparent samples. The CSLM can be used to form a three-dimensional image of any sample.

PRINCIPLE OF OPERATION

A schematic representation of a confocal scanning laser microscope is shown in Figure 8. A beam of laser light is reflected by a dichroic mirror and focused onto a spot within the sample by the objective lens. Dichroic mirrors reflect light of one wavelength and transmit that of another wavelength. A laser beam illuminates the sample at the focus of the objective lens and excites fluorescence in the focused spot. The sample then emits light at a lower wavelength, which goes through the objective, passes through the dichroic mirror, and is focused down to another diffraction-limited spot, which is surrounded by a narrow pinhole. The pinhole is said to be confocal to the focal point of the objective lens on the sample because it is positioned at a point conjugate to the focal point of objective lens. The pinhole spatially filters out light originating from parts of the sample not focused by the laser beam. Light from the focused spot of the sample is then passed to the detector. The laser beam is focused at different portions of the sample to cover a range of depths. This allows point-by-point construction of the three-dimensional image of the sample (Lu, 2005).

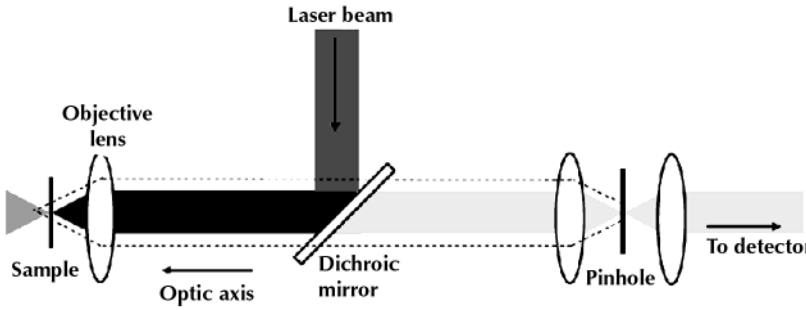

FIGURE 8 A schematic representation of a confocal scanning laser microscope (adapted from Lu, 2005).

PREPARATION OF SAMPLES

Preparation of samples for CSLM requires use of a staining agent for differentiating different phases and ingredients. Staining agent can be applied by either covalent or non-covalent labeling. Covalent labeling involves covalent linking of a fluorescent dye to the desired sample. Non-covalent labeling involves addition of fluorescent dye to the sample. For non-covalent labeling, fluorescent dye with affinity for either hydrophilic or hydrophobic regions can be used. Rhodamine B, a dye with affinity for hydrophilic region, is used to stain aqueous solution of proteins. Dyes with affinity for hydrophobic regions include Nile red and Nile blue A (Tromp et al., 2004).

Bio-nanocomposites based on layered clay can be stained with Safranine O by ion-exchange. Safranine O, a fluorescent dye, contains aluminum ion. Aluminum ion enables this dye to intercalate in clay galleries during ion-exchange. Confocal microscopy can then be used to determine the extent of dispersion of clay during mixing or sonication (Yoonessi et al., 2004).

COLLECTION AND INTERPRETATION OF DATA

The CSLM image can be used to evaluate the extent of mixing on micrometer scale. The CSLM image can be reconstructed to yield an image giving a three-dimensional impression of the sample. The three-dimensional image provides better insight into the extent of mixing on micrometer scale in the sample.

LIMITATIONS

One of the main limitations of CSLM is the requirement for a florescent dye which can bind to the region of interest. The resolution (~130 nm) of CSLM is poorer than that of TEM (Yoonessi et al., 2004). Therefore, CSLM analysis should always be used in combination with other microscopic techniques such as TEM or AFM.

13.4 SPECTROSCOPY

Spectroscopy is the study of the interaction between electromagnetic radiation and a material as a function of wavelength. Spectroscopy is used to determine functional

groups, structural conformation, and concentration of different components in a material. The main spectroscopy techniques used for structural characterization of bionanocomposites are Fourier transform infra-red (FTIR), Raman, and nuclear magnetic resonance (NMR) spectroscopy.

13.4.1 FOURIER TRANSFORM INFRA-RED (FTIR) SPECTROSCOPY

Infra-red (IR) radiation is a part of the electromagnetic spectrum with wavelength ranging from 0.8 to 100 μm. The region of infra-red radiation is further sub-divided into near infra-red (0.8–2.5 μm), mid infra-red (2.5–15 μm), and far infra-red (15–100 μm). Typical wavenumber (1/wavelength) for mid infra-red spectroscopy ranges from 400–4000 cm^{-1}. The energy associated with absorption of IR radiation promotes rotation and vibration of chemical bonds. This vibrational energy is related to the strength of the bond and the molecular mass. The IR spectroscopy measures the absorption of specific frequencies of IR radiation by a sample. The measured absorption can be used to identify chemical bonds or functional groups in a particular sample. The IR spectroscopy uses high resolution diffraction monochromator for generating the absorption spectrum. This results in long measurement time because the absorption at each wavelength is measured sequentially. Another alternative form of IR analysis is Fourier transform infra-red spectroscopy. The FTIR spectroscopy uses an interferometer instead of a monochromator to measure absorption at all wavelengths simultaneously. The FTIR spectrometer is also fast and more sensitive as compared to a conventional IR spectrometer (Reh, 2001).

PRINCIPLE OF OPERATION

A schematic representation of an FTIR spectroscope is shown in Figure 9. The IR radiation is produced by heating an inert solid such as silicon carbide to 1,000–1,800°C. An interferometer consists of a beam splitter and two mirrors (fixed mirror and moving mirror). The beam splitter, which is a semi-reflecting device, is made by depositing a thin film of germanium onto a flat potassium bromide (KBr) substrate. The beam splitter divides the IR radiation in two beams: one beam is transmitted to the fixed mirror and the other beam is reflected to the moving mirror. When the two beams recombine after being reflected from the two mirrors, they undergo constructive and destructive interference due to the optical path difference between them. The optical path difference is created by varying the relative position of the moving mirror with respect to the fixed mirror. This recombined IR radiation is passed through the sample. Fluctuation in the intensity of energy at the detector is digitized into an interferogram. An interferogram contains time-domain spectrum (intensity *vs*. time) over the entire IR region. The interferogram is converted into a conventional frequency domain spectrum (intensity *vs.* frequency) using Fourier transform (Sherman-Hsu, 1997).

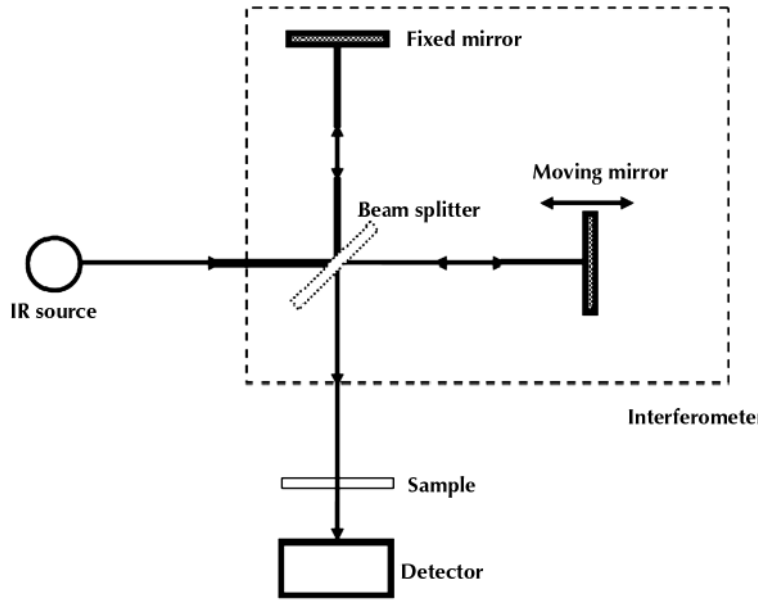

FIGURE 9 A schematic representation of an FTIR spectroscope (adapted from Sherman-Hsu 1997).

PREPARATION OF SAMPLES

Any solid, liquid, or gas sample can be analyzed using FTIR spectroscopy. The most common method to prepare solid samples involves use of a matrix to disperse the ground sample. The matrix can be a liquid (mineral oil) or solid (potassium bromide). For a liquid matrix, the paste of the ground sample and the liquid is spread between two IR transparent windows. For a solid matrix, a mixture of ground sample and potassium bromide (KBr) is pressed under high pressure (~80 MPa) for a few minutes. Recrystallization of KBr results in a clear disk, which can be inserted into the optical beam with a special sample holder. Liquids are analyzed as thin films in a cell with two IR transparent windows. A Teflon spacer is generally used to produce a film of the desired thickness (Reh, 2001).

Another method to prepare samples is based on attenuated total reflectance (ATR). The ATR device measures the total reflected energy from the surface of a sample in contact with an IR transmitting crystal. The refractive index of the crystal is significantly higher than that of the sample. This ensures total internal reflection of the radiation in the crystal. Infra-red radiation penetrates a small distance into the sample before reflecting back to the crystal. Therefore, there should be good optical contact between the sample and the crystal. Many solid samples give very weak spectra because the contact is confined to small areas (Reh, 2001).

COLLECTION AND INTERPRETATION OF DATA

The spectrum for a particular sample is obtained by plotting the intensity of % transmitted radiation as a function of wavenumber. Many functional groups absorb IR radiation in a very narrow range of wavenumber. The spectrum obtained from an FTIR analysis can be used to either determine the presence of a functional group in a sample or compare the spectrum of unknown material to that of known reference material (ASTM Standards, 1998).

Strong absorption bands appear in the region of 4000–2500 cm^{-1} because of the stretching vibrations between hydrogen and atoms with molecular weight (M) less than 19. Absorption bands in the region of 2700–1850 cm^{-1} usually appear because of triple bonds (C≡N) and other functional groups such as S-H, P-H, and Si-H. Many double bonded functional groups show absorption bands in the region of 1950–1450 cm^{-1}. Some of those double bonded functional groups include carbonyl groups, ketones, aldehydes, carboxylic acids, amides, and esters (Sherman-Hsu 1997). Absorption bands corresponding to C=O stretching (amide I), N-H bending (amide II), and C-N stretching (amide III) occur at 1630 cm^{-1}, 1530 cm^{-1}, and 1230 cm^{-1} respectively (Schmidt et al., 2005).

Absorption bands from stretching of silicon oxygen bonds (Si-O) occur in the region of 950–1100 cm^{-1}. This is particularly important for layered clay-based bio-nanocomposites because Si-O bonds are present in clay. The absorption band for agglomerated clay layers (tactoids) is broad. The absorption band becomes narrower as the degree of exfoliation increases. Thus, FTIR spectroscopy can be used to determine the extent of exfoliation in bio-nanocomposites (Klein et al., 2005). Absorption bands associated with different bonds of montmorillonite are shown in Table 1.

TABLE 1 Absorption spectra associated with montmorillonite (Chen et al., 2001)

Wavenumber (cm^{-1})	Functional groups
3627	Stretching vibration of-OH bond
3429	Stretching of interlayer H_2O
1635	Deformation of interlayer H_2O
1091 and 1039	Stretching of Si-O
519 and 466	Stretching of Al-O and bending of Si-O

LIMITATIONS

The FTIR spectroscopy can only be used to analyze samples, which are transparent to IR radiation. Multiple functional groups can absorb IR radiation in the same range of wavenumber. Therefore, this technique should be complemented with other analytical techniques such as Raman or nuclear magnetic resonance (NMR) spectroscopy (Sherman-Hsu, 1997).

Raman spectroscopy involves radiating a sample with monochromatic visible of near infra-red light from a laser. While IR spectroscopy detects the change in dipole moment, Raman spectroscopy detects change in polarizability of a sample. Some of the advantages of Raman spectroscopy over IR spectroscopy include ease of sample preparation, faster analysis, and better spatial resolution. However, heat generated by the laser in Raman spectroscopy may change the characteristics of the sample during measurement (Thygesen et al., 2003).

13.4.2 NUCLEAR MAGNETIC RESONANCE (NMR) SPECTROSCOPY

Nuclear magnetic resonance (NMR) is a phenomenon which occurs when the nuclei of certain atoms, under a static magnetic field (B_0), are exposed to a second oscillating magnetic field (B_1). The NMR spectroscopy can be performed on materials which have a net nuclear spin due to unpaired protons or neutrons. The unpaired proton or neutron with a spin generates a tiny magnetic field with a magnetic moment, μ. The alignment of the spin with the external magnetic field can result in either a low energy or a high energy configuration. There can be a transition between the two energy configurations by absorption (low to high energy configuration) or emission (high to low energy configuration) of a photon. The energy of the photon is equal to the difference between the two energy levels. The signal in NMR spectroscopy is obtained from the difference in energy absorbed and emitted. Thus, the NMR signal is proportional to the population difference between the two energy states. At room temperature, the number of spins in low energy level is slightly greater than those in high energy level. The NMR spectroscopy is sensitive enough to detect this small difference between the number of spins in low and high energy levels (Keeler, 2006).

PRINCIPLE OF OPERATION

A schematic representation of an NMR spectroscope is shown in Figure 10. A superconducting magnet (superconducting solenoid immersed in liquid helium) generates a static magnetic field (B_0) within the sample in the z-direction. Shim coils are used to maintain the homogeneity of the magnetic field. The sample tube is a cylindrical metal tube inserted into the bore of the magnet. The magnetic moments (μ) of all the spins in a sample can be represented by a net magnetization vector ($M = \sum\mu = M_x i + M_y j + M_z k$). At equilibrium, the net magnetization vector ($M_z = M_0$, $M_x = M_y = 0$) lies along the direction of B_0 (z-direction). The value of B_0 is much greater than M_0. Therefore, it is not possible to detect the net magnetization vector of the sample. If the magnetization vector is tilted away from the z-axis by an angle β, it precesses around the z-axis and sweeps out a cone with an angle β.

The frequency (ν in rad s^{-1}) of precession is given by (Keeler 2006):

$$\nu = \gamma B_0 \quad \backslash^* \text{ MERGEFORMAT} \tag{5}$$

where γ, unique to each isotope, is the gyromagnetic ratio.

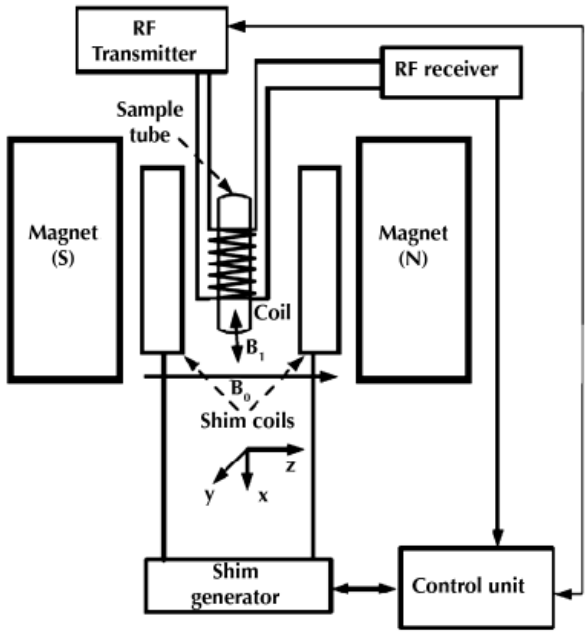

FIGURE 10 A schematic representation of an NMR spectroscope (adapted from Keeler 2006).

The values of γ for proton (^{1}H) and Carbon-13 (^{13}C) are 42.58 and 10.71 MHz/Tesla respectively. The frequency ν is also known as the resonance or Larmor frequency. Tilting of the magnetization vector is achieved by applying a very small oscillating magnetic field (B_1) along the x-axis. This oscillating secondary magnetic field is generated by transmitting radio frequency (RF) waves through a radio frequency (RF) coil. The response of the magnetization vector to this alternating field is used to receive signals in NMR spectroscopy. Resonance is achieved when the frequency of B_1 is equal to the Larmor frequency. Once resonance is achieved, the magnetization vector will precess about the x-axis with a frequency (ν_1) given by (Keeler, 2006):

$$\nu_1 = \gamma B_1$$

For a typical NMR experiment, B_1 is much smaller than B_0. Therefore, ν_1 is smaller than the Larmor frequency (ν). A pulsed magnetic field along the x-axis is produced by switching on and off the RF field in the coil. Pulse time (τ) is the duration of time the field is on. The pulse field rotates the magnetization vector about the x-axis by a certain angle, known as the flip angle (β). Flip angle is given by (Keeler 2006):

$$\beta = 2\pi\nu_1\tau \quad \backslash^* \text{ MERGEFORMAT} \qquad (7)$$

A pulse field giving a flip angle of β is known as a β pulse. The most common flip angles are 90° and 180°. A 90° pulse rotates the magnetization vector from its equilibrium position to the negative y-axis. A 180° pulse, known as the inversion pulse, rotates net magnetization vector from positive z-axis to negative z-axis (Keeler, 2006). Rotation axis of the pulse can be changed by changing the phase offset (φ) of the RF field.

After the magnetization vector has been flipped by the RF pulse, transverse magnetization (M_{xy}) relaxes back to zero and longitudinal magnetization (M_z) relaxes back to its equilibrium value (M_0). Longitudinal or spin-lattice relaxation constant (T_1) is the time required for the longitudinal magnetization vector (M_z) to return to 63% of its equilibrium value (M_0). T_1 is also the time required by the spins to exchange energy with the surrounding lattice. The longitudinal relaxation time is most commonly measured by using an inversion recovery pulse sequence. In an inversion recovery pulse sequence, a 180° pulse is followed by a delay (τ) and a 90° pulse. Duration of the delay is longer than the duration of either the 180° pulse or 90° pulse. If the magnetization vector is placed in x-y plane, it will precess about the z-axis at the Larmor frequency. Along with precession, M_{xy} also starts to decay to its equilibrium value of zero because of the heterogeneity of magnetic field and molecular interactions. Transverse or spin-spin relaxation time (T_2) is the time required to reduce M_{xy} by a factor of e (~2.718). In the absence of a heterogeneous magnetic field, T_2 can be estimated by a spin echo pulse sequence. In a spin echo pulse sequence, a 90° pulse is followed by a delay (τ), a 180° pulse, and another delay (τ). The signal is acquired after the second delay. T_2 is always less than T_1 (Keeler, 2006).

The NMR signal is detected as an induced oscillating voltage (μV) in the RF coil by the RF receiver. The same RF coil is used for both exciting the spins and detecting the signal. The RF transmitter and receiver are separated by a device, known as diplexer. A diplexer is a fast acting switch which connects the receiver to the coil only when the transmitter is disconnected. The NMR signal is detectable only for a short duration because it decays due to the above mentioned relaxation processes. The decaying time-domain signal is known as the free induction decay (FID) signal. An analog to digital convertor (ADC) converts the signal from a voltage to a binary number. Fourier transform of the FID signal produces a spectrum with intensity as a function of frequency (Keeler, 2006).

PREPARATION OF SAMPLES

During sample preparation for NMR spectroscopy, the sample tubes should be clean and free of any contaminants. The sample should be dry and free of any solvent. The NMR samples are prepared by dissolving the sample in a solvent containing deuterium. The most common solvent is deuterated chloroform. The sample should be completely dissolved in the solvent because undissolved particles can distort the homogeneity of the magnetic field.

COLLECTION AND INTERPRETATION OF DATA

The NMR spectrum is a plot of intensity as function of frequency. A typical range for frequency is from 10 to 800 MHz. The NMR results are also expressed on a chemical shift scale. The chemical shift scale is set up by defining the peak frequency (ν_{ref}) from tetramethylsilane (TMS) as zero.

The chemical shift (δ) is defined as (Keeler 2006):

$$\delta = 10^6 \times \frac{\left(\nu_p - \nu_{ref}\right)}{\nu_{ref}} \backslash * \text{ MERGEFORMAT} \quad (8)$$

where ν_p is the frequency of the peak intensity for a sample. The chemical shift is often expressed in parts per million (ppm).

The FID signal decays quicker in solids as compared to liquids. Thus, the shape of the FID signal can be used to distinguish between solid and liquid components of a sample. The relaxation times T_1 and T_2 provide information about the molecular structures of compounds (Choi et al., 2003). The values of T_1 and T_2 depend on the magnetic field, type of nucleus, temperature, and presence of other larger molecules. The value of T_1 for nuclei bound to larger molecules such as proteins is much lower than that for nuclei bound to pure water.

Some studies on the use of NMR for structural characterization of bio-nanocomposites have been reported (Avella et al., 2005; Bruno et al., 2008). Bruno et al., (2008) investigated the molecular structure and intermolecular interaction between the components of bio-nanocomposites based on poly(3-hydroxybutyrate) (PHB) and modified MMT using NMR. Values of T_1 were determined for the bio-nanocomposites at different MMT content. Results showed that NMR can be used as an efficient and rapid method to characterize the structures of bio-nanocomposites.

LIMITATIONS

The main limitation of NMR spectroscopy is its sensitivity. Atomic nuclei which have high sensitivity to NMR can only be analyzed by NMR spectroscopy. The NMR spectroscopy can only be used for a non-paramagnetic sample.

CONCLUDING REMARKS

This chapter reviews analytical techniques for the structural characterization of biopolymer-based nanocomposites. Selection of proper technique for characterization of these bio-nanocomposites is very critical in assessing their performance. The XRD is generally used as the preferred technique to determine immiscible or intercalated arrangements of nanoparticles in bio-nanocomposites. The SEM can be used as a quick method to study the dispersion of larger aggregates (~1 μm) of nanoparticles at the surface of a bio-nanocomposite. The TEM images can provide a qualitative understanding of the internal structure, spatial distribution, and dispersion of nanoparticles in bio-nanocomposites. The TEM in conjunction with XRD can provide information on the occurrence and degree of intercalation or exfoliation in bio-nanocomposites. The AFM can be used to study the structure as well as mechanical properties of a surface at the nano-scale. Spectroscopy techniques (FTIR and NMR) can be used in conjunction with microscopy techniques to obtain information on the interaction between nanoparticles and the biopolymer matrix.

Future studies on the characterization techniques need to focus on development of:

1. Microscopy techniques capable of obtaining three-dimensional images,
2. Better and faster methods of sample preparation,

3. Better image analysis techniques for better interpretation of results, and
4. Microscopy at elevated temperature.

These future developments will help in better understanding of the interaction between nanoparticles and biopolymer matrix. This will aid in the synthesis of bio-nanocomposites with improved properties.

KEYWORDS

- **Biopolymer-based nanocomposites**
- **X-ray diffraction**
- **Scanning electron micrsocopy**
- **Tunneling electron microscopy**
- **Atomic force microscopy**
- **Fourier-transform infra-red spectroscopy**
- **Nuclear magnetic resonance**

REFERENCES

1. ASTM Standards. E1252-98. General techniques for obtaining infrared spectra for qualitative analysis. Philadelphia, PA (1998).
2. Avella, M., Vlieger, J. J. D., Errico, M. E., Fischer, S., Vacca, P., and Volpe, M. G. Biodegradable starch/clay nanocomposite films for food packaging applications. *Food Chemistry*, **93**, 467–474 (2005).
3. Bhushan, B. Scanning probe microscopy: Principle of operation, instrumentation, and probes. B. Bhushan, (Ed.), *Springer Handbook of Nanotechnology* Springer, New York, pp. 325–369 (2004).
4. Bordes, P., Pollet, E., and Averous, L. Nano-biocomposites: biodegradable polyester/nanoclay systems. *Progress in Polymer Science*, **34**(2), 125–155 (2009).
5. Bozzola, J. J. and Russell, L. D. *Electron microscopy: principles and techniques for biologists*. Jones & Bartlett Publishers, Boston (1999).
6. Bruno, M., Tavares, M. I. B., Motta, L. M., Miguez, E., Preto, M., and Fernandez, A. O. R. Evaluation of PHB/clay nanocomposites by spin-lattice relaxation time. *Materials Research*, **11**(4), 483–485 (2008).
7. Chavaria, F. and Paul, D. R. Comparison of nanocomposites based on nylon 6 and nylon 66. *Polymer*, **45**(25), 8501–8515 (2004).
8. Chen, G., Liu, S., Chen, S., and Qi, Z. FTIR spectra, thermal properties, and dispersibility of a polystyrene/montmorillonite nanocomposite. *Macromolecular Chemistry and Physics*, **202**, 1189–1193 (2001).
9. Chen, P. and Zhang, L. Interaction and properties of highly exfoliated soy protein/montmorillonite nanocomposites. *Biomacromolecules*, **7**, 1700–1706 (2006).
10. Choi, S. G, Kim, K. M., Hanna, M. A., Weller, C. L., and Kerr, W. L. Molecular dynamics of soy-protein isolate films plasticized by water and glycerol. *Journal of Food Science*, **68**(8), 2516–2522 (2003).
11. Dennis, H. R., Hunter, D. L., Chang, D., Kim, S., White, J. L., Cho, J. W., and Paul, D. R. Effect of melt processing conditions on the extent of exfoliation in organoclay-based nanocomposites. *Polymer*, **42**, 9513–9522 (2001).

12. Dimonie, D., Constantin, R., Vasilievici, G., Popescu, M. C., and Garea, S. The dependence of the XRD morphology of some bio-nanocomposites on the silicate treatment. *Journal of Nanomaterials*, (2008). doi:10.1155/2008/538421.
13. Egerton, R. F. *Physical principles of electron microscopy: an introduction to TEM, SEM, and AEM*. Springer, New York (2005).
14. Guiannuzzi, L. A. and Stevie, F. A. A review of focused ion beam milling techniques for TEM specimen preparation. *Micron*, **30**(3), 197–204 (1999).
15. Jia, J. F, Yang, W. S, and Xue, Q. K.. Scanning tunneling microscopy. N. Yao and Z. L. Wang (Eds.). *Handbook of Microscopy for Nanotechnology*, Springer, New York, pp. 55–112 (2005).
16. Jinnai, H. and Spontak, R. J. Transmission electron microtomography in polymer research. *Polymer,* **50**, 1067–1087 (2009).
17. Ivanov, D. A., Amalou, Z, and Magonov, S. N. Real-Time evolution of the lamellar organization of poly(ethylene terephthalate) during crystallization from the melt: high-temperature atomic force microscopy study. *Macromolecules*, **34**, 8944-8955 (2001).
18. Kasai, K. Kakudo, M. *X-ray diffraction by macromolecules, Springer*, New York, p. 504 (2005).
19. Keeler, J. *Understanding NMR spectroscopy*, John Wiley & Sons Inc., New Jersey, p.459 (2006).
20. Klein, R. J., Benderly, D. Kemnetz, A., and Ijdo, W. L. A new methods to determining the quality of smectite clay/plastic nanocomposites: degree of nanodispersion and clay layer alignment. Nanocomposites 2005 fifth world congress, San Franciscso, California, USA (Aug 22–24, 2005)
21. Koo, J. H. Polymer nanocomposites: processing, characterization, and applications, McGraw-Hill, New York, p. 272 (2006).
22. Lu, P. J. Confocal scanning optical microscopy and nanotechnology. N, Yao and Z. L Wang (Eds.). *Handbook of Microscopy for Nanotechnology*. Springer, New York, pp. 3–24 (2005).
23. Magonov, S. N. and Yerina, N. A. Visualization of nanostructures with atomic force microscopy. N. Yao, Z. L. Wang, (Eds.). *Handbook of Microscopy for Nanotechnology*, Springer, New York, pp. 113–155 (2005).
24. Magonov, S. N. and Reneker, D. H. Characterization of polymer surfaces with atomic force microscopy. *Annual review of materials science*, **27**, 175–222 (1997).
25. Marsh, K. and Bugusu, B. Food packaging: roles, materials, and environmental issues. *Journal of food science*, **72**(3), R39–R55 (2007).
26. McGlashan, S. A. and Halley, P. J. Preparaion and characterization of biodegradable starch-based nanocomposite materials. *Polymer international*, **52**, 1767–1773 (2003).
27. Monticelli, O. Musina, Z. Russo, S., and Bals, S. On the use of TEM in the characterization of nanocomposites. *Materials letters*, **61**, 3446–3450 (2007).
28. Morgan, A. B. and Gilman, J. W. Characterization of polymer-layered silicate (clay) nanocomposites by transmission electron microscopy and X-ray diffraction: a comparative study. *Journal of applied polymer science*, **87**, 1329–1338 (2003).
29. **Nam, P. H., Maiti, P., Okamoto, M. Kotaka, T. Hasegawa, N., and Usuki, A.** A hierarchical structure and properties of intercalated polypropylene/clay nanocomposites. Polymer, 42(23), 9633–9640 (**2001).**
30. Pandey, J. K., Kumar, A. P, Misra, M., Mohanty, A. K, Drzal, L. T., and Singh, R. P. Recent advances in biodegradable nanocomposites. *Journal of nanoscience and nanotechnology*, **5**, 497–526 (2005).
31. Paul, D. R. and Robeson, L. M. Polymer nanotechnology: nanocomposites. *Polymer*, **49**, 3187–3204 (2008)
32. Pavlidou, S, Papaspyrides, C. D. A review on polymer-layered silicate nanocomposites. *Progress in polymer science*, **33**, 1119–1198 (2008).
33. Ray, S. S. and Bousmina, M. Biodegradable polymers and their layered silicate nanocomposites: In greening the 21st century materials world. *Progress in materials science*, **50**, 962–1079 (2005).
34. Reh, C. In-line and off-line FTIR measurements. E. Kress-Rogers and C. J. B Brimelow (Eds). *Instrumentation and Sensors for the Food Industry*, CRC Press, Boca Raton, pp. 213–232 (2001).

35. Rhim, J. W. and Ng, P. K. W. Natural biopolymer-based nanocomposite films for packaging applications. *Critical reviews in food science and nutrition*, **47**(4), 411–433 (2007).
36. Schmidt, V. Giacomelli, C. and Soldi, V. Thermal stability of films formed by soy protein isolate-sodium dodecyl sulfate. *Polymer degradation and stability*, **87**, 25–31 (2005).
37. Shabeer, A. Chandrashekhara, K. and Schuman, T. Synthesis and characterization of soy-based nanocomposites. *Journal of composite materials*, **41**(15), 1825–1849 (2007).
38. Sherman-Hsu, C. P. Infrared spectroscopy. F. Settle (Ed.). *Handbook of Instrumental Techniques for Analytical Chemistry*, Prentice Hall PTR, New Jersey, pp. 247–283 (1997).
39. Sorrentino, A. Gorrasi, G., and Vittoria, V. Potential perspectives of bio-nanocomposites for food packaging applications. *Trends in food science and technology*, **18**, 84–95 (2007).
40. Tang, X., Alavi, S., and Herald, T. J. Effects of plasticizers on the structure and properties of starch–clay nanocomposite films. *Carbohydrate polymers*, **74**, 552–558 (2008).
41. Thygesen, L. G, Lokke, M. M. Micklander, E. and Engelsen, S. B. Vibrational microspectroscopy of food. Raman vs. FTIR. *Trends in food science and technology*, **14**, 50–57 (2003).
42. Tromp, R. H., Nicolas, Y., Van de Velde, F., and Paques, M. Confocal scanning laser microscopy (CSLM) for monitoring food composition. I. E. Tothill (Ed.). *Rapid and On-line Instrumentation for Food Quality Assurance*, CRC Press, Boca Raton, pp. 306–323 (2003).
43. Vaz, C. M., Mano, J. F., Fossen, M., Van Tuil, R. F., De Graaf, L. A., Reis, R. L., and Cunh, A. M.. Mechanical, dynamic-mechanical, and thermal properties of soy protein-based thermoplastic with potential biomedical applications. *Journal of macromolecular science – physics*, **B41**(1), 33–46 (2002).
44. Vermogen A. Masenelli-Varlot, K. Sgula, R Duchet-Rumeau, J. Boucard, S., and Prele, P. Evaluation of the structure and dispersion in polymer-layered silicate nanocomposites. *Macromolecule*s, **38**(23), 9661–9669 (2005).
45. Wang, Z. L. New developments in transmission electron microscopy for nanotechnology. *Advanced materials*, **15**(18), 1497–1514 (2003).
46. Williams, D. B. and Carter C. B. T*ransmission electron microscopy: a textbook for materials science*. Springer, New York. p. 721 (1996).
47. Yalcin B and Cakmak, M. The role of plasticizer on the exfoliation and dispersion and fracture behavior of clay particles in PVC matrix: a comprehensive morphological study. *Polyme*r, **45**, 6623–6638 (2004).
48. Yang, K. K., Wang, X. L. and Wang, Y. Z. Progress in nanocomposite of biodegradable polymer. *Journal of industrial and engineering chemistry*, **13**(4), 485–500 (2007).
49. Yao, N. Focused ion beam systems – a multifunctional tool for nanotechnology. N. Yao and Z. L. Wang (Eds.), *Handbook of Microscopy for Nanotechnology*, Springer, New York, pp. 247–286 (2005).
50. Yoonessi, M. Toghiani, H. Kingery, W. L., and Pittman, C. U. Preparation, characterization, and properties of exfoliated/delaminated organically modified clay/dicyclopentadiene resin nanocomposites. *Macromolecules*, **37**(7), 2511–2518 (2004).
51. Yu, J, Cui, G, Wei, M, and Huang, J. Facile exfoliation of rectorite nanoplatelets in soy protein matrix and reinforced bio-nanocomposites thereof. *Journal of applied polymer science*, **104**, 3367–3377 (2007).
52. Zeng, Q. H., Yu, A. B., Lu, G. Q., and Paul, D. R. Clay-based polymer nanocomposites: research and commercial development. *Journal of nanoscience and nanotechnology*, **5**, 1574–1592 (2005).
53. Zhao, R, Torley, P., and Halley, P. J. Emerging biodegradable materials: starch- and protein-based bio-nanocomposites. *Journal of materials science*, **43**, 3058–3071 (2008).